# Generalized and Reduced Analytical Formulation for Ultra-Fast 3-D Field and Vector Potential Calculation from Arch-Shaped Axially Magnetized Bodies in Electrical Machines

Frederic Maurer[1], Basile Kawkabani[1], *Senior Member, IEEE*, and Jonas Kristiansen Nøland[2], *Member, IEEE*
[1] Ecole Polytechnique Federale de Lausanne, Station 17, CH-1015 Lausanne, Switzerland
[2]Department of Electric Power Engineering, Norwegian University of Science and Technology, Trondheim, Norway

**Arch-shaped axially magnetized bodies tend to appear frequently in electrical machine analysis such as in overhang parts of classical radial-flux machines as well as in main parts of axial-flux machines. The calculation of 3-D fields originating from these bodies is demanding. 3-D FEA suffers from high computational burden as well as no knowledge of the field origin. Analytic techniques involve the use of elliptic integrals and complex numbers for numerical evaluation, which makes them significantly slower than 3-D FEA.**

**In this paper, a new analytical technique is proposed to speed up the computation by factor 20 for the global magnetic field created by a generic magnetized body, by removing complex numbers and reducing the analytic equations significantly without any loss of precision. As a result, it can compete with conventional 3-D FEA. In addition, integral methods may contribute to the wider use of parallel processing techniques. The original expressions for the vector potential are also provided, which has its own benefits and applications. Finally, the showcased magnetized body is assessed against 3-D FEA and discussed in terms of practical applications.**

***Index Terms*—Arched magnets, 3-D magnetic fields, cylindrical coordinates, analytical formulation, non-linear magnetized bodies, integral calculation, vector potential, permanent magnets (PMs), supra-conductive coils.**

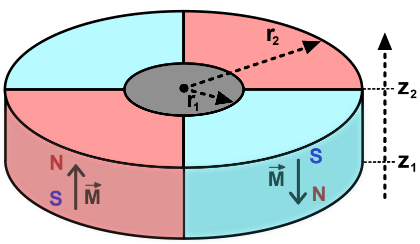


Fig. 1: Example of a multipole generic axially magnetized body in free space with radial and axial parameters corresponding to the nomenclature ($r_1$, $r_2$, $z_1$, $z_2$ and $\vec{M}$).

## I. Nomenclature

The nomenclature of this paper is adopted from well-known terminology [1], where the variables are described in the following.

1) $\varphi_1$, $\varphi_2$, $\phi = \varphi - \varphi'$, and $\alpha$ [defined in eq. (9)] are angles [rad].
2) $r_1$, $r_2$, $r$, and $r'$ are radial distances [m]
3) $\gamma = z' - z$, $z_1$, $z_2$, $z$, and $z'$ are axial distances [m].
4) $\vec{H}$ (magnetic field) is the $\vec{H}$-field in this paper [A/m].
5) $\vec{B}$ (magnetic flux density) is $\vec{B}$-field in this paper [T].
6) $\vec{A}$ (magnetic vector potential) is the $\vec{A}$-field in this paper [Wb/m].
7) $\vec{M}$ (magnetization vector) is the $\vec{M}$-field in this paper [T].

Fig. 3 defines the quantities and subscripts geometrically.

Manuscript received July 5, 2019; revised January 3, 2020 and February 25, 2020; accepted April 28, 2020. Corresponding author: F. Maurer (e-mail: frederic.maurer@me.com).

## II. Introduction

The computation of sophisticated 3-D $\vec{H}$-fields and $\vec{A}$-fields is a classical problem in electrical machine analysis. This field problem can be divided into separate contributions, one originating from coils. The other one is the contribution from magnetized bodies (in particular arch-shaped in this paper) that tend to appear in the machine geometries (e.g., machine overhangs). In particular, the combination of radial and axial fields appear as an edge-effect in the classical radial-flux machines [2]–[5]. Overhang structures can sometimes be used to increase the flux density in the air gap. For a detailed analysis, it is normal to distinguish between different overhang parts and non-overhang regions [6]–[8]. Fig. 1 depicts a generic axially magnetized overhang segment of a classical four-pole machine. In axial flux machines, the 3-D fields become more dominant along the path of the main magnetic circuit [9]–[14]. Moreover, the halbach-type axial-flux machines [11]–[14] use smaller arch-shaped permanent magnets (PMs) interacting with ferromagnetic materials and embedded coils. Slotless structures of axial-flux machines are analyzed [13], [14], with or without back-iron. They use magnetic disks made by arch-shaped PMs, which could also be depicted by the generic body of Fig. 1.

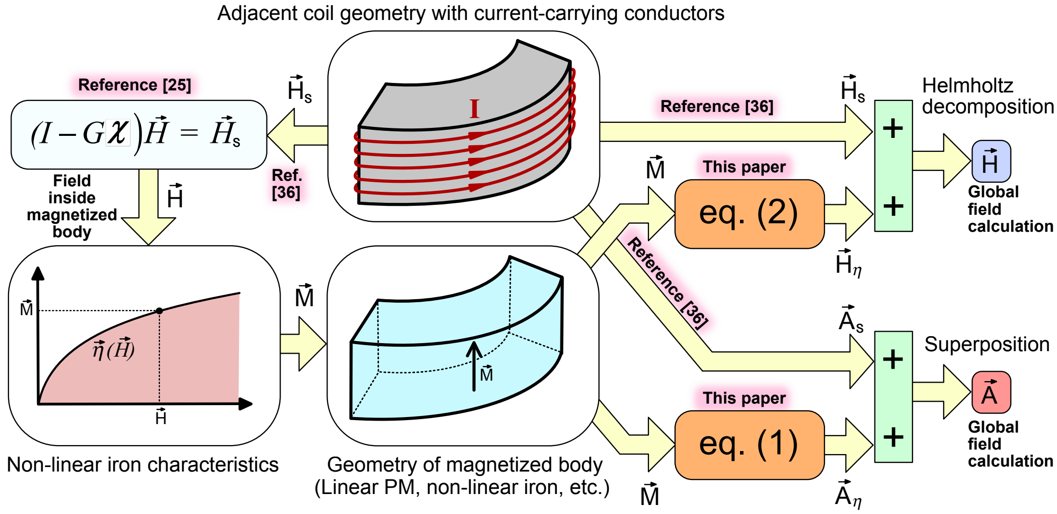


Fig. 2: Flowchart depicting the calculation of the global 3-D magnetic field from arch-shaped axially magnetized bodies. The methodology highlights how to interface them with adjacent windings or other external magnetization sources.

In general, analytical methodologies are needed for efficient design optimization of electrical machines [15]–[18] as they have a lower memory requirement than 3D-FEA. In addition, they yield "on-demand" calculation[1] and they provide knowledge of the field origin. Several methodologies have been proposed, including the integral field calculation method [19], the green's functions method [20] and the Bessel functions method [21], [22]. Still, the computational complexity of such analytic techniques is high. In general, the $\vec{A}$-field is overlooked in these methods. What's more, there exist generalized methodologies that can be extended to not only cover linear PMs but to any general magnetizable body (such as iron parts and non-linear PMs) [23], [24] as it will be explained in the next paragraph. So, these novel analytic formulae for both the 3-D $\vec{H}$-fields and $\vec{A}$-fields constitute the pavement for many application cases of advanced analysis in electrical machines [7].

Magnetized bodies containing ferromagnetic materials need to take the non-linear iron saturation into account. A method has been developed [25], which requires the computation of the magnetic field generated for a given magnetization. In [25], the magnetic field ($\vec{B}$) is conventionally defined as $\vec{B} = \mu_0(\vec{H} + \vec{M})$, where $\vec{M}$ is the magnetization vector, which can origin from a linear material ($\vec{M} = \mu_0(\mu_r - 1)\vec{H}$) or from remanent flux density, $\vec{B}_r = \mu_0\mu_r\vec{H}_c$ where $\vec{B} = \mu_0\mu_r\vec{H} + \vec{B}_r$, or from a ferromagnetic material with non-linear characteristic ($\vec{M} = \eta(\vec{H})$). In this particular case, [25] details an algorithm with known current-carrying conductors (coils). This is for example the case in PMs and a non-linear magnetizable iron. Compared to 3-D FEA, the method developed in [25] permits to obtain the $\vec{A}$-field produced by a given magnetization using only scalar potentials for each node instead of a $\vec{A}$-field for each node for the 3-D FEA approach which is significantly reducing the memory needed for such computations.

The practical implementation of these novel formulae uses the elliptic integral calculation algorithms developed in [26]–[28], which reduces the calculation time by at least one order of magnitude compared to published methods [29].

### A. Literature Review on Analytical Field Computation

Extensive work has been devoted to the 3-D $\vec{H}$-field calculation problem, while the literature on the 3-D $\vec{A}$-field calculation is more sparse in comparison, due to its prior limited practical applications. However, the $\vec{A}$-field is a very practical variable in field simulations, due to its straightforward relationship to the induced voltage.

In general, there are two main models used to compute the $\vec{H}$-field and $\vec{A}$-field of magnetized bodies, namely, the Colombian approach [30] and the Amperian approach [31]. There are some possible simplifications of the analytic formulas for the $\vec{H}$-field, namely, a 2-D approximation [32]. Moreover, the $\vec{H}$-field can be calculated using Heuman's Lambda function [33] or using separation of variables in polar coordinates applied to magnetic gears [34]. Selvaggi [35] introduce a $\vec{H}$-field calculation employing toroidal harmonics.

### B. Contributions of this paper

This paper advocates the need for an analytic approach for a rapid and precise numerical field computation of elliptic integrals [26]–[28]. Novel simplified integral field calculation

[1] An "on-demand" calculation is a calculation, where only the needed field points are computed. The calculation is done on the requested points, while a finite-element calculation requires the computation to be done on the complete mesh, even if one is interested only in the result at some points.

expressions are proposed to take full advantage of the hybrid analytic-numerical model, thus reducing significantly the computational costs. As demonstrated in the introduction, our approach using a generic arch-shaped magnetized body (see Fig. 3) allow to represent a wide range of machine problems. The speed-up of the proposed novel equation for the $\vec{H}$-field is due to the following improvements:

1) The number of equations in the formulation of the magnetic equations is reduced from 12 to 6.
2) No complex numbers are employed in the calculation, which reduces the computation costs since the evaluation of imaginary values is strictly avoided.

### C. Outline

The remainder of the paper is organized as follows. In Section III, the basic integrals for the generic problem are briefly presented. In Section IV, the novel reduced expressions are derived. In Section V, the expressions are evaluated in a generalized case study. Finally, Section VI concludes the paper.

## III. Basic Integrals Describing a Magnetized Body

This section introduces the theoretical fundamentals of a generic arch-shaped magnetized body that are typically found in electrical machine analysis. In addition, basic integrals for the novel reduced magnetic expressions of the body are introduced.

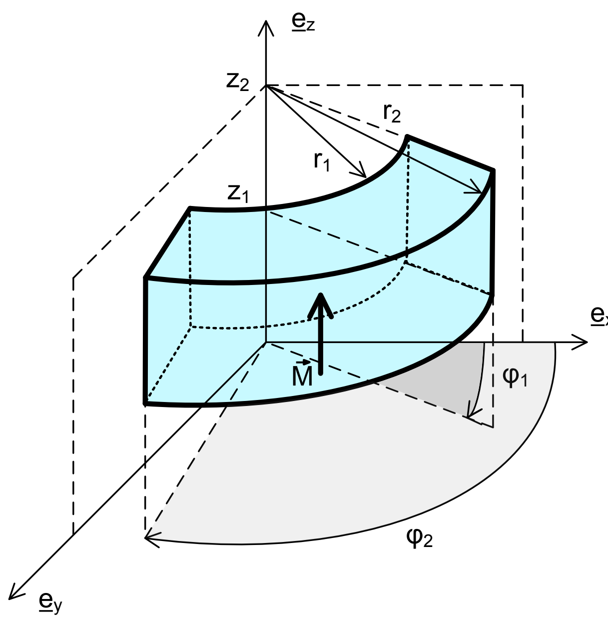


Fig. 3: Schematic representation of a primitive magnetized body with $\vec{M}$ in cylindrical coordinates where $\underline{e}_x = \vec{e}_x$.

Fig. 3 depicts a generic arch-shaped magnetizable body using the nomenclature of Section I. It is presented in cylindrical coordinates as well as the definitions and denominations of the used variables. $\vec{M}$ is the constant magnetization vector, which is oriented along $\vec{e}_z$. It coincides with $\vec{e}_{z'}$, the local (or source) axial unitary vector of the coordinate system ($r'$,$\phi$,$z'$). The global coordinate system is given by ($r$,$\varphi$,$z$).

The integral $\int_\phi$ is taken over the tangential coordinate $\phi$ of the local cylindrical coordinate system (integration over $\phi = \varphi - \varphi_1$ to $\phi = \varphi - \varphi_2$). Similarly, $\int_r \int_z$ is the surface integral over the radial and axial coordinates $r'$ (integration over $r = r_1$ to $r = r_2$) and $z'$ (integration over $z = z_1$ and $z = z_2$) of the local (or source) cylindrical coordinate system. In the calculation, $\vec{r}$ is the vector to the point where the potential vector respectively field is calculated, while $\vec{r}'$ is a vector pointing to a point located in the source volume to be integrated (refer to Fig. 3) and $\mu_0$ the permeability of the vacuum ($4\pi 10^{-7}$ N/$A^2$). Refer to Section I for the definition of the variables used in this article.

The magnetization ($\vec{M}$) have been considered as uniformly constant to stay within the same hypothesis as "usually" employed in the literature (refer to [31], [36]–[38] among others). This leads to comparable results with older contributions, for the sake of fairness. It is possible to take a non-constant magnetization into account by dividing the magnetized body into smaller domains, with a constant magnetization over each sub-domain.

In deriving the $\vec{A}$-field as a function of the $\vec{M}$-field, there is only one expression [39], is not very easy to use in the case of an analytic integration. This formula can be simplified using a "curl" version of the integration [39] by parts, yielding

$$\vec{A}(\vec{r}) = \frac{1}{4\pi} \iiint_V \frac{\vec{\nabla}' \times \vec{M}(\vec{r}')}{|\vec{r} - \vec{r}'|} dV' + \frac{1}{4\pi} \iint_{\partial V} \frac{\vec{M} \times \vec{d\sigma}'}{|\vec{r} - \vec{r}'|}. \tag{1}$$

which is used in this paper.

In the case of an axially magnetized body with constant magnetization, its divergence as well as its rotation are null, so that the Amperian approach is chosen, leading to a direct integration to obtain the $\vec{H}$-field. The basic equations for the $\vec{H}$-field then become

$$\vec{H}(\vec{r}) = \frac{1}{4\pi\mu_0} \iiint_V \frac{\left(\vec{\nabla}' \times \vec{M}(\vec{r}')\right) \times \left(\vec{r} - \vec{r}'\right)}{|\vec{r} - \vec{r}'|^3} dV' + \frac{1}{4\pi\mu_0} \iint_{\partial V} \frac{\left(\vec{M}(\vec{r}') \times \vec{n}\right) \times \left(\vec{r} - \vec{r}'\right)}{|\vec{r} - \vec{r}'|^3} \tag{2}$$

where $\vec{n}$ is the normal unit vector pointing out of the surface $\partial V$ of the volume V.

## IV. Novel reduced analytic expressions

This section derives the proposed novel generic expressions for a primitive magnetized body from first principles of integral field calculation. First, the mathematical transformations are given. Then, the $\vec{H}$-field and $\vec{A}$-field is treated in separate subsections.

### A. Mathematical variables and transformations

The following additional variables (namely B, D, G, $\beta_1$, $\beta_2$ and $\beta_3$), which have been defined in [1] and will be used in the mathematical development hereafter.

$$B^2(\phi) = r^2 + r'^2 - 2rr'\cos(\phi) \tag{3}$$
$$D^2(\phi) = \gamma^2 + B^2(\phi) \tag{4}$$
$$G^2(\phi) = \gamma^2 + r^2\sin(\phi) \tag{5}$$
$$\beta_1(\phi) = (r' - r\cos(\phi))/G(\phi) \tag{6}$$
$$\beta_2(\phi) = \gamma/B(\phi) \tag{7}$$
$$\beta_3(\phi) = \gamma(r' - r\cos(\phi))/[r\sin(\phi)D(\phi)]. \tag{8}$$

The integrals along the tangential coordinate are transformed into elliptic integrals. An angle transformation is used [1], which is defined by

$$\phi = \pi - 2\alpha. \tag{9}$$

Moreover, the elliptic integral coefficients are formulated

$$k^2 = \frac{4rr'}{\gamma^2 + (r+r')^2} \tag{10}$$
$$a^2 = \gamma^2 + (r+r')^2 \tag{11}$$
$$n^2 = \frac{4rr'}{(r+r')^2}. \tag{12}$$

These constants and the angle transformation lead to the following expressions

$$\begin{aligned} B^2(\alpha) &= r^2 + r'^2 - 2rr'\cos(\phi) \\ &= (r+r')^2(1 - n^2\sin(\alpha)^2) \end{aligned} \tag{13}$$
$$D^2(\alpha) = \gamma^2 + B^2(\phi) = a^2(1 - k^2\sin(\alpha)^2). \tag{14}$$

In addition, $G(\phi)$ will be expressed as

$$G^{-2}(\alpha) = \frac{1}{2\sqrt{\gamma^2+r^2}}\Big(\frac{1}{(\sqrt{\gamma^2+r^2}-r)(1-n_1^2\sin(\alpha)^2)} \tag{15}$$
$$+ \frac{1}{(\sqrt{\gamma^2+r^2}+r)(1-n_2^2\sin(\alpha)^2)}\Big),$$

where

$$n_1^2 = \frac{2r}{r - \sqrt{\gamma^2+r^2}} \tag{16}$$
$$n_2^2 = \frac{2r}{r + \sqrt{\gamma^2+r^2}}. \tag{17}$$

### B. Improved equations for the magnetic field ($\vec{H}$-field)

In this subsection, eq. (3) will be further modified. Replacing $|\vec{r} - \vec{r}'|$ by $D(\phi)$, using the fact that the magnetization is considered to be only along the z-axis and that the divergence of the magnetization is null, lead to the following expression to be integrated

$$\vec{H}(r,\varphi,z) = \frac{M}{4\pi\mu_0}\int_{\varphi_1}^{\varphi_2} d\phi \int_{r_1}^{r_2} dr' \frac{r'}{D(\phi)^3}\begin{pmatrix} r - r'\cos(\phi) \\ -r'\sin(\phi) \\ \gamma \end{pmatrix}\Bigg|_{z'=z_1}^{z'=z_2}, \tag{18}$$

where $D(\phi)$ is given by eq. (4) and is a function of $r'$ and $z'$ but these two variables are not mentioned explicitly to stay consistent with the notation defined in [1].

[36] integrates eq. (18), but its expressions for the radial and axial component differs from this paper. It has been possible to find novel analytic expressions requiring the calculation of fewer elliptic integrals of the third kind and without the usage of complex numbers for both components. The tangential component has the same expression as in [36].

To obtain the improved analytic expressions, integrate over the angle $\phi$ is needed, integrating the expressions only once per part. The formulas for the *sine*-function and further *cosine*-function of the double of the argument are utilized to obtain the compact expressions. The radial component ($H_r$) and the axial component ($H_z$) are treated in separated subsection.

#### 1) Radial magnetic field ($H_r$-component)

Starting from the radial component of eq. (18), first an integration over $r'$ is done. One obtains

$$\begin{aligned} H_r =& \frac{M}{4\pi\mu_0}\int_{\varphi_1}^{\varphi_2} d\phi \int_{r_1}^{r_2} dr' r' \frac{r - r'\cos(\phi)}{D(\phi)^3}\Big|_{z'=z_1}^{z'=z_2} \\ =& \frac{M}{4\pi\mu_0}\int_{\varphi_1}^{\varphi_2} d\phi \frac{r(r^2+\gamma^2 - rr'\cos(\phi))}{G^2(\phi)D(\phi)} \\ &+ \frac{\cos(\phi)(r'(\gamma^2 - r^2\cos(2\phi)) + r(r^2+\gamma^2)\cos(\phi))}{G^2(\phi)D(\phi)} \\ &- \cos(\phi)\sinh^{-1}\Big(\beta_2(\phi)\Big)\Big|_{r'=r_1}^{r'=r_2}\Big|_{z'=z_1}^{z'=z_2}. \end{aligned} \tag{19}$$

This integral is composed of two terms: $I_{r1}$ and $I_{r2}$, where the term $\frac{M}{4\pi\mu_0}$ have been omitted (i.e., $H_r = \frac{M}{4\pi\mu_0}(I_{r1} + I_{r2})$). The first term can be converted to an elliptic integral. One obtains

$$\begin{aligned} I_{r1} =& \int_{\varphi_1}^{\varphi_2} d\phi \frac{r(r^2+\gamma^2 - rr'\cos(\phi))}{G^2(\phi)D(\phi)} \\ &+ \frac{\cos(\phi)(r'(\gamma^2 - r^2\cos(2\phi)) + r(r^2+\gamma^2)\cos(\phi))}{G^2(\phi)D(\phi)} \\ =& -2\int_{\alpha_1}^{\alpha_2} d\alpha \frac{\alpha_0 + \alpha_2\sin(\alpha)^2 + \alpha_4\sin(\alpha)^4 + \alpha_6\sin(\alpha)^6}{G^2(\alpha)D(\alpha)}, \end{aligned} \tag{20}$$

which can be computed using the formulas of [40] and numerically evaluated using the algorithms developed in [26]–[28]. For $I_{r2}$, using one integration by parts leads to

$$\begin{aligned} I_{r2} =& -\int_{\varphi_1}^{\varphi_2} d\phi \Big[ \cos(\phi)\sinh^{-1}\Big(\beta_2(\phi)\Big)\Big] \\ =& -\sin(\phi)\sinh^{-1}\Big(\beta_2(\phi)\Big)\Big|_{\phi=\varphi_1-\varphi}^{\phi=\varphi_2-\varphi} \\ & \underbrace{-rr'\gamma\int_{\varphi_1}^{\varphi_2} d\phi \quad \frac{\sin(\phi)}{B^2(\phi)D(\phi)}}_{\mathrm{I}}. \end{aligned} \tag{21}$$

The remaining integral I (highlighted in Eq. 21) will be transformed into an elliptic integral

$$\begin{aligned} I =& -rr'\gamma\int_{\varphi_1}^{\varphi_2} d\phi \quad \frac{\sin(\phi)}{B^2(\phi)D(\phi)} \\ =& \frac{8\gamma rr'}{(r+r')^2 a}\int_{\alpha_1}^{\alpha_2} d\alpha \quad \frac{\sin(\alpha)^2-\sin(\alpha)^4}{(1-n^2\sin(\alpha)^2)\sqrt{1-k^2\sin(\alpha)^2}}. \end{aligned} \tag{22}$$

These elliptic integrals can also be solved using the formulas of [40] and numerically evaluated using the algorithms developed in [26]–[28].

*2) Axial magnetic field ($H_z$-component)*

For the axial component of the $\vec{H}$-field given by eq. (18), first an integration over $r'$ is performed. The obtained expression can be directly transformed into an elliptical integral, which is solved using the formulas of [40] and numerically evaluated using the algorithms developed in [26]–[28], yielding

$$\begin{aligned} H_z =& \frac{M}{4\pi\mu_0}\int_{\varphi_1}^{\varphi_2} d\phi\int_{r_1}^{r_2} dr' \frac{\gamma r'}{D(\phi)^3}\Big|_{z'=z_1}^{z'=z_2} \\ =& -\frac{M\gamma}{4\pi\mu_0}\int_{\varphi_1}^{\varphi_2} d\phi \frac{r^2-r'r\cos(\phi)+\gamma^2}{G^2(\phi)D(\phi)}\Big|_{r'=r_1}^{r'=r_2}\Big|_{z'=z_1}^{z'=z_2} \\ =& \frac{2M\gamma}{4\pi\mu_0}\int_{\alpha_1}^{\alpha_2} d\alpha \frac{\alpha_0+\alpha_2\sin(\alpha)^2}{G^2(\alpha)D(\alpha)}\Big|_{r'=r_1}^{r'=r_2}\Big|_{z'=z_1}^{z'=z_2}. \end{aligned} \tag{23}$$

As a result, the total number of elliptic integrals of the third kind to be computed has been reduced to 6 compared to 12 in [36]. In addition, there are no more complex numbers to evaluate inside the expressions, which also reduces the computational time as well.

### C. Original development for the vector potential ($\vec{A}$-field)

For the $\vec{A}$-field presented in Section III, one starts with eq. (1), then replaces $|\vec{r} - \vec{r}'|$ by $D(\phi)$ and then compute the needed vector products. In the considered case of an axial magnetization, the $\vec{A}$-field fundamental integrals given by eq. (1) can be reduced to the following integrals to be computed analytically

$$\begin{aligned} \vec{A} =& \frac{\mu_0 M}{4\pi}\int_{r_1}^{r_2} dr'\int_{z_1}^{z_2} dz' \frac{1}{D(\phi)}\begin{pmatrix}-1\\0\\0\end{pmatrix}\Big|_{\phi=\varphi_1-\varphi}^{\phi=\varphi_2-\varphi} \\ & + \frac{\mu_0 M}{4\pi}\int_{\varphi_1}^{\varphi_2} d\phi\int_{z_1}^{z_2} dz' \frac{r'}{D(\phi)}\begin{pmatrix}\sin(\phi)\\ \cos(\phi)\\0\end{pmatrix}\Big|_{r'=r_1}^{r'=r_2}. \end{aligned} \tag{24}$$

This subsection first develops the expressions for the radial component ($A_r$) and then for the tangential component ($A_\phi$), utilizing eq. (25).

*1) Radial vector potential ($A_r$-component)*

The first integral of the radial component becomes

$$\begin{aligned} A_r =& -\frac{\mu_0 M}{4\pi}\int_{r_1}^{r_2} dr'\int_{z_1}^{z_2} dz' \frac{1}{D(\phi)}\Big|_{\phi=\varphi_1-\varphi}^{\phi=\varphi_2-\varphi} \\ =& -\frac{\mu_0 M}{4\pi}\int_{z_1}^{z_2} dz' \sinh^{-1}\Big(\beta_2(\phi)\Big)\Big|_{r'=r_1}^{r'=r_2}\Big|_{\phi=\varphi_1-\varphi}^{\phi=\varphi_2-\varphi} \\ =& -\frac{\mu_0 M}{4\pi}\Big(-\gamma + r\sin(\phi)\Big)\tan^{-1}\Big(\frac{\gamma}{r\sin(\phi)}\Big) \\ & - r\sin(\phi)\tan^{-1}\Big(\beta_3(\phi)\Big) + \gamma\sinh^{-1}\Big(\beta_1(\phi)\Big) \\ & + \Big(r' - r\cos(\phi)\Big)\sinh^{-1}\Big(\beta_2(\phi))\Big)\Big|_{r'=r_1}^{r'=r_2}\Big|_{\phi=\varphi_1-\varphi}^{\phi=\varphi_2-\varphi}\Big|_{z'=z_1}^{z'=z_2}. \end{aligned} \tag{25}$$

The second integral of the radial component can be easily integrated performing first an integration over $d\phi$ and then $dz'$ resulting in very simple analytic functions.

*2) Angular vector potential ($A_\varphi$-component)*

The integral for the tangential component is solved integrating first over $dz'$ and then $d\phi$. One obtains after integration over $dz'$

$$A_\varphi = \frac{\mu_0 M}{4\pi}\frac{1}{2}r'^2\int_{\varphi_1}^{\varphi_2} d\phi \quad \cos(\phi)\sinh^{-1}\Big(\beta_2(\phi)\Big) \tag{26}$$

The integration will be done using integration by parts leading to

$$\begin{aligned} A_\varphi =& \frac{\mu_0 M}{4\pi}\frac{1}{2}r'^2\int_{\varphi_1}^{\varphi_2} d\phi \quad \cos(\phi)\sinh^{-1}\Big(\beta_2(\phi)\Big) \\ =& \frac{\mu_0 M}{4\pi}\frac{1}{2}r'^2\sin(\phi)\sinh^{-1}\Big(\beta_2(\phi)\Big) \\ & + \frac{\mu_0 M}{4\pi}\frac{1}{2}\underbrace{r'^3 r\int_{\varphi_1}^{\varphi_2} d\phi \quad \frac{\sin(\phi)^2}{B^2(\phi)D(\phi)}}_{\mathrm{Y}}. \end{aligned} \tag{27}$$

The last integral can be transformed into an elliptic integral denoted $Y$ (highlighted in Eq. 27)

$$\begin{aligned} Y &= -r'^3 r \int_{\varphi_1}^{\varphi_2} d\alpha \quad \frac{4\sin(\alpha)^2(1-\sin(\alpha)^2)}{B^2(\alpha)D(\alpha)} \\ &= -r'^3 r \int_{\varphi_1}^{\varphi_2} d\alpha \quad \frac{4\sin(\alpha)^2(1-\sin(\alpha)^2)}{B^2(\alpha)D(\alpha)} \\ &= -r'^3 r \int_{\varphi_1}^{\varphi_2} d\alpha \quad \frac{4\sin(\alpha)^2 - 4\sin(\alpha)^4}{B^2(\alpha)D(\alpha)}, \end{aligned} \tag{28}$$

which can be numerically evaluated using the algorithms developed in [26]–[28]. In fact, the case considering $r = 0$ is trivial and leads to simple analytic expressions.

## V. Validations for a Magnetized Body

This section verifies the expressions of Section IV for case studies of the arch-shaped axially magnetized body, without any claim to represent exact elements of a particular machine overhang segment or any other geometry. Some overhang parts are usually approximated with axial magnetization to simplify the analysis. For the sake of simplicity, only one arch-segment was considered in the validation. However, according to the principle of superposition, a complete overhang geometry could be extrapolated from the same approach. In addition, the varying impact of the magnetization vector from adjacent windings could also be included (as outlined in Fig. 2).

In emulating a realistic scenario, an axial constant magnetization vector inside the body was picked to corresponding to a remanent flux density of 1 Tesla. It is a common value used in many publications (refer to [36]–[38] among others). No suitable TEAM-problem was identified for the magnetic body geometry and earlier investigations did not provide accurate enough data for replicability purposes [36]. As a consequence, this paper follows a similar methodological validation approach, as presented in [41] for the $\vec{H}$-field and one for the $\vec{A}$-field. For the $\vec{H}$-field, the 3-D FE results were obtained with a converging solution, i.e., the mesh density was incrementally increased until the final value is settled for the 5 to 7 digits precision in some key points. For the $\vec{A}$-field, there were lack of computational resources, but the validation inside the body was of particular focus.

First, the proposed $\vec{H}$-field calculation is validated in Section V-A. Then, a case study of improved computational speed is presented in Section V-B. Finally, the $\vec{A}$-field is validated in Section V-C.

### A. Validation of the $\vec{H}$-field using 3-D FE simulations

The 3-D FE simulations of this subsection use the scalar approximation with global cartesian field quantities. The comparison is made for the body defined in Fig. 3 with parameters specified in Table I (a given constant and uniform remanent magnetization of 1 Tesla in the axial direction). The validation paths are defined in Section VII.

Figs. 4 and 6 show the results of the comparison for the $\vec{H}$-field calculation, while Figs. 5 and 7 present the relative difference between the analytic computation and the numerical simulation. All curves indicate excellent agreement with 3-D FE, which clearly validates the predictability of the novel analytic expressions of the $\vec{H}$-field.

TABLE I: Specification of the magnetized body used in the case study to validate the magnetic field ($\vec{H}$-field) with 1 Tesla remanent magnetization.

| Parameter | Description | Value | Unit |
|---|---|---|---|
| $r_l$ | Inner radius | 350 | mm |
| $r_2$ | External radius | 650 | mm |
| $\varphi_1$ | First tangential angle | -$\pi$/4 | rad |
| $\varphi_2$ | Second tangential angle | $\pi$/4 | rad |
| $z_l$ | Lower axial component | -250 | mm |
| $z_2$ | Upper axial component | 250 | mm |

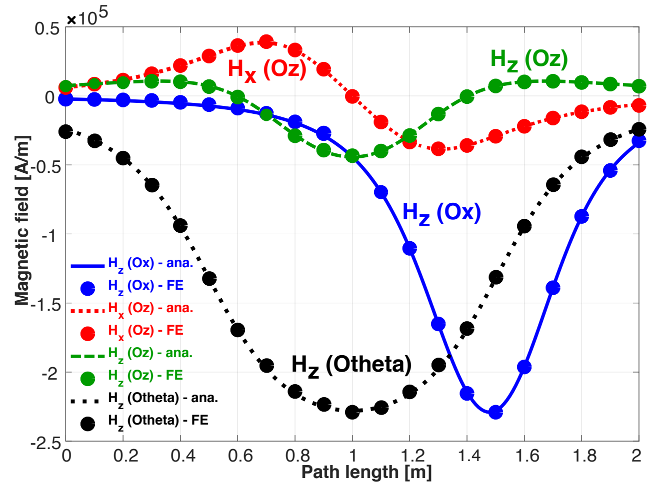


Fig. 4: Comparison between analytic formulas ($\vec{H}$-field) and 3-D FE calculation on different paths (defined in Section VII-B and in Fig. 11) with a uniform axial $\vec{M}$ in a magnetized body (refer to Fig. 3 and Table I for the specification).

TABLE II: Mean value of the $\vec{H}$-field difference for the magnetized body (Table I) one different paths (defined in Fig. 11) as per Figs. 4 and 6 with 1 Tesla uniform remanent magnetization.

| Component | Path | Difference (A/m) |
|---|---|---|
| $H_z$ | Ox | 636.58 |
| $H_x$ | Oz | 244.89 |
| $H_z$ | Oz | 283.10 |
| $H_z$ | Otheta | 911.64 |
| $H_x$ | Diag | 920.27 |
| $H_y$ | Diag | 823.48 |
| $H_z$ | Diag | 926.82 |

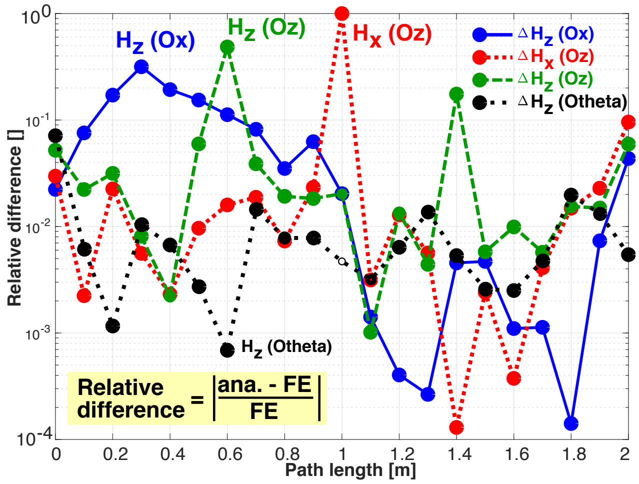


Fig. 5: Relative difference between analytic formulas ($\vec{H}$-field) and 3-D FE calculation on different paths (defined in Section VII-B and in Fig. 11) with a uniform axial $\vec{M}$ in a magnetized body (refer to Fig. 3 and Table I for the specification).

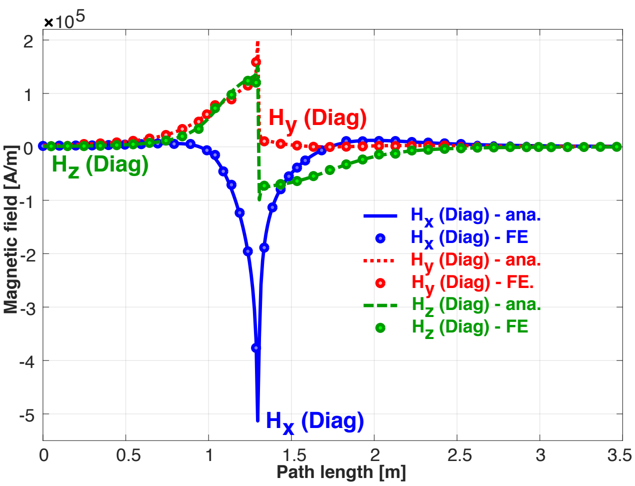


Fig. 6: Comparison between analytic formulas ($\vec{H}$-field) and 3-D FE calculation on different paths (defined in Section VII-B and in Fig. 11) with a uniform axial $\vec{M}$ in a magnetized body (refer to Fig. 3 and Table I for the specification).

Table II present the mean value of the $\vec{H}$-field difference for the cases shown in Figs. 4 and 6. The mean value is significantly higher for Diag as the path passes through point singularities which are difficult to catch using FE computation. For the other cases, the mean value is low and could be improved using a denser mesh, but it would be beyond the computing power of the laboratory.

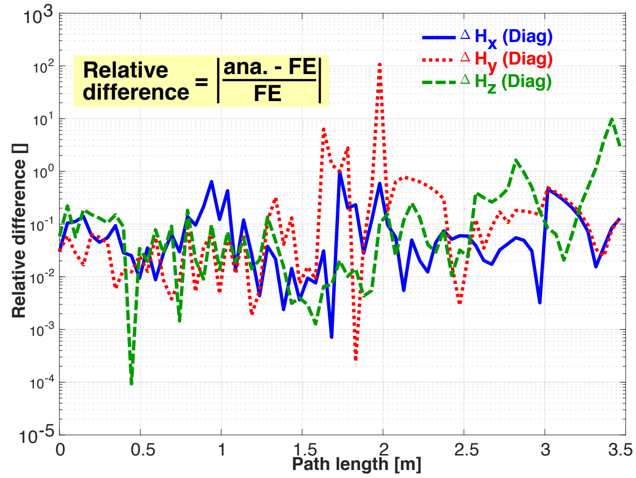


Fig. 7: Relative difference between analytic formulas ($\vec{H}$-field) and 3-D FE calculation on different paths (defined in Section VII-B and in Fig. 11) with a uniform axial $\vec{M}$ in a magnetized body (refer to Fig. 3 and Table I for the specification).

### *B. Computational speed case study for the $\vec{H}$-field*

This subsection is dedicated to highlighting the improvement in computational speed as a result of the novel formulation without complex numbers and with less elliptic integrals. A case study based on the magnetized body defined in table III is done comparing the computational speed of the novel formulas presented in this paper and the formulas presented in [36] on the ten validation paths defined in section VII-B and depicted in Fig. 11. The computations have been performed in the Matlab environment, applying Fukushima's calculation methods for this work, while the built-in functions have been used for the equations developed in [36] as they contain complex numbers. The computer has four cores and 16GB RAM. The results of the case study are shown in Fig. 8. The computation time is different depending on the chosen path, as they have a different number of points (refer to the caption of Fig. 8).

The case study reveals a speed increase of about factor 20, which demonstrates the advantage of the novel formulas compared to the ones published in [36]. The reduced computational time is due to the reduction of the number of elliptic integrals and the Fukushima method to compute the elliptic integrals.

### *C. Validation of the $\vec{A}$-field using both 3-D FE simulations and numerical integration*

Finally, this subsection validates the $\vec{A}$-field expression in a two-step approach. First, from numerical integration and then with comparison against 3D-FEA. Numerical integration of the integral expression is assessed against the novel analytic expression. They are compared in Table IV, where $A_r$ and $A_\varphi$ are evaluated from both methods. The differences are very small

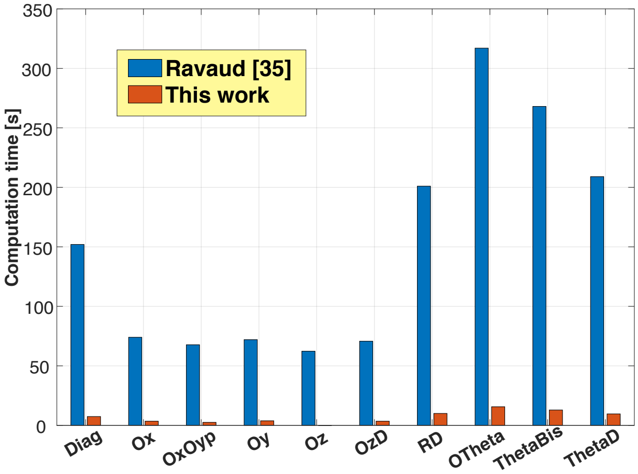


Fig. 8: Case study on the reduced computation time of the $\vec{H}$-field using the novel formulas. Diag and RD have 351 points, Theta and its variation has 751 points while the other path have only 201 points. The computer had 4 cores and 16GB RAM.

TABLE III: Specification of the magnetization body used in the case study to validate the vector potential ($\vec{A}$-field) numerically and to assess the computational speed. The numerical value of the parameters is derived from the one used in [36].

| Parameter | Description | Value | Unit |
|---|---|---|---|
| $r_l$ | Inner radius | 25 | mm |
| $r_2$ | External radius | 28 | mm |
| $\varphi_1$ | First tangential angle | -$\pi$/8 | rad |
| $\varphi_2$ | Second tangential angle | $\pi$/8 | rad |
| $z_l$ | Lower axial component | 0 | mm |
| $z_2$ | Upper axial component | 3 | mm |

for both components, around 100 times the double machine precision ($\epsilon = 1.11e^{-16}$). This step confirms the exactitude of the novel expressions.

In a second validation step, the expression is assessed against a 3-D FE simulation using the $\vec{A}$-field formulation. In fact, the challenge is that the 3-D FE leads to high memory requirements even for small simulation volumes. As a result, the second step focused the computational resources on achieving a good precision inside the magnetic body, with outliers outside due to courser mesh. The inherent memory limitations of the computer laboratory are challenging when working with a three-component vector field for numerical computation.

The curves are compared with a 3-D FEA, where the magnetized body parameters (refer to Fig. 3) is also defined in Table I. The curves (refer to Figs. 9 and 10) for the $\vec{A}$-field has a higher errors outside the magnetic body due to the coarser mesh outside. The curves match quantitatively inside and qualitatively outside along the validation paths. The 3-D FEA is very memory intensive as they require four-node

TABLE IV: Simplified sample assessment of magnetized body (Table II) with an observer located at $(r, \varphi, z) = (0.024m, 0rad, 0.0015m)$ with 1 Tesla uniform remanent magnetization.

| Comp. | Equation | Analytic eval. | Numerical int. | Dev. |
|---|---|---|---|---|
| $A_r$ | Eq. (25) | 0.018797279Wb/m | 0.018797279Wb/m | $< 100\epsilon$ |
| $A_\varphi$ | Eq. (26) | 0.919063950Wb/m | 0.919063950Wb/m | $< 100\epsilon$ |

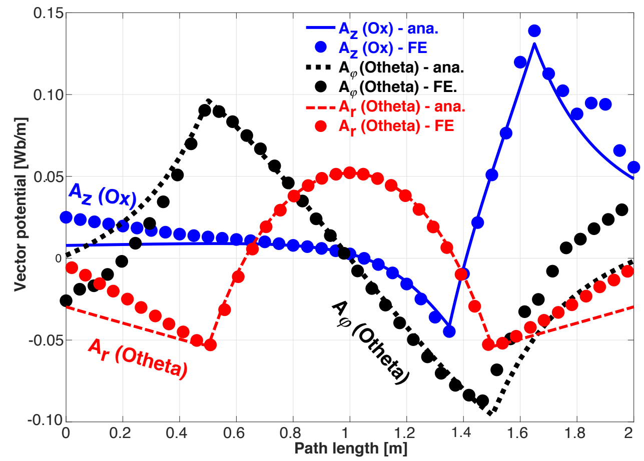


Fig. 9: Comparison between analytic formulas ($\vec{A}$-field) and 3-D FE calculation on different paths (defined in Section VII-B and in Fig. 11) with a uniform axial $\vec{M}$ in a magnetized body (refer to Fig. 3 and Table I for the specification).

vector elements to compute the $\vec{A}$-field potential, which limits the maximal number of nodes due to the limited computing power available at the laboratory.

The curves of Fig. 10 are worth considering as they provide a sense for the numerical precision of the 3D-FEA. Theoretically, the curves shall all be equal to zero, also at the edges of the validation paths. Finally, the analytic expressions of eqs. (25) and (26) can be considered as validated because numerical integration reveals a very good quantitative agreement and the 3-D FE agrees well inside the magnetic body.

## VI. Conclusion

This article showcases the utility of an improved 3-D integral field computation method of the $\vec{H}$-field and the $\vec{A}$-field originating from arch-shaped magnetized bodies, which constitutes the pavement for many applications in electrical machines. A peculiar case study confirms the superiority of the proposed analytic formulations in comparison with alternative approaches [36]. Moreover, validity of the expressions has been assessed in the 3-D FEA environment. The main highlights of the paper are the following.

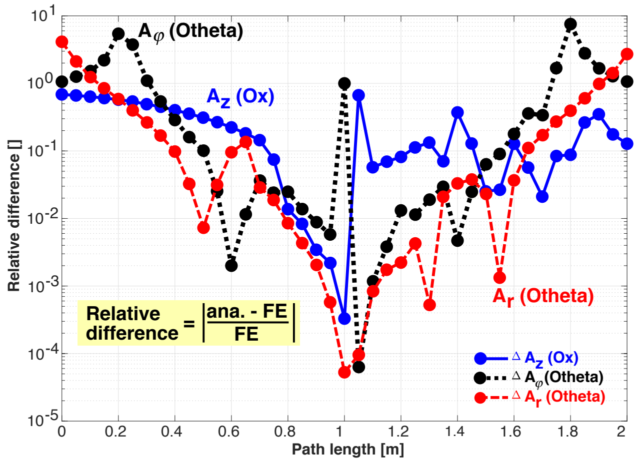


Fig. 10: Relative difference between analytic formulas ($\vec{A}$-field) and 3-D FE calculation on different paths (defined in Section VII-B and in Fig. 11) with a uniform axial $\vec{M}$ in a magnetized body (refer to Fig. 3 and Table I for the specification).

1) The novel expressions for the $\vec{H}$-field reduces the number of elliptic integrals from 12 to 6 and with no need for complex numbers.
2) The numerical speed-up of about factor 20 is achieved utilizing the algorithms developed by Fukushima and was shown in a case study of the $\vec{H}$-field.
3) In addition, the expressions for the $\vec{A}$-field have been validated against numerical integration, and they present an error below 100 times double machine precision ($\epsilon$). In addition, they have been assessed quantitatively against 3-D FE.

This paper combines two advancements, namely, our novel equations and the algorithms of Fukushima. As a result, this work enables advanced 3-D electrical machine analysis with low memory requirement and computational time. In addition, the individual contributions of each magnetized body can be easily identified. The ”on-demand” calculation provides the field quantities only at the needed locations, thus reducing also the computational needs in obtaining any given result.

The original expressions for the $\vec{A}$-field are a fundamental contribution paving the way to a wider application of integral methods such as hybridizing 3-D integral field overhang models with 2-D FE core models in transient simulations of electrical machines [7]. Moreover, they can be used for ultra-fast parametric studies of diverse overhang lengths and parts in radial flux machines or for efficient optimizations in axial-flux machines.

Future works will handle the $\vec{A}$-field expression for the radial and the tangential magnetization in a way that a magnetic element with any magnetization can be modelled.

# VII. Appendix

## A. Case of $r = 0$

In the case $r = 0$ one gets

$$\begin{aligned} H_r &= -\frac{M}{4\pi\mu_0}\int_{\varphi_1}^{\varphi_2} d\phi \int_{r_1}^{r_2} dr' \frac{r'^2\cos(\phi)}{D(\phi)^3}\Big|_{z'=z_1}^{z'=z_2} \\ &= -\frac{M}{4\pi\mu_0}\sin(\phi)\left(\sinh^{-1}\left(\frac{r'}{\gamma}\right) - \frac{r'}{\sqrt{\gamma^2+r'^2}}\right)\Big|_{r'=r_1}^{r'=r_2}\Big|_{\phi=\varphi_1-\varphi}^{\phi=\varphi_2-\varphi}\Big|_{z'=z_1}^{z'=z_2} \end{aligned} \tag{29}$$

In the case $r = 0$ one gets

$$\begin{aligned} H_z &= \frac{M}{4\pi\mu_0}\int_{\varphi_1}^{\varphi_2} d\phi \int_{r_1}^{r_2} dr' \frac{\gamma r'}{(\gamma^2+r'^2)^{3/2}}\Big|_{z'=z_1}^{z'=z_2} \\ &= -\frac{M\gamma}{4\pi\mu_0}\phi\frac{1}{\sqrt{\gamma^2+r'^2}}\Big|_{r'=r_1}^{r'=r_2}\Big|_{\phi=\varphi_1-\varphi}^{\phi=\varphi_2-\varphi}\Big|_{z'=z_1}^{z'=z_2}. \end{aligned} \tag{30}$$

When $r = 0$ ones gets

$$\begin{aligned} A_r &= \frac{\mu_0 M}{4\pi}\int_{r_1}^{r_2} dr' \int_{z_1}^{z_2} dz' \frac{1}{\sqrt{\gamma^2+r'^2}}\Big|_{\phi=\varphi_1-\varphi}^{\phi=\varphi_2-\varphi} \\ &= \frac{\mu_0 M}{4\pi}\phi\Big|_{\phi=\varphi_1-\varphi}^{\phi=\varphi_2-\varphi}\int_{z_1}^{z_2} dz' \sinh^{-1}\left(\frac{r'}{|\gamma|}\right)\Big|_{r'=r_1}^{r'=r_2} \\ &= \frac{\mu_0 M}{4\pi}\phi\left(r'\sinh^{-1}\left(\frac{\gamma}{r'}\right) + \gamma\sinh^{-1}\left(\frac{r'}{|\gamma|}\right)\right)\Big|_{r'=r_1}^{r'=r_2}\Big|_{\phi=\varphi_1-\varphi}^{\phi=\varphi_2-\varphi}\Big|_{z'=z_1}^{z'=z_2} \end{aligned} \tag{31}$$

## B. Validation paths

The magnetic field is compared on ten paths which are given by the following expressions

$$\mathrm{Ox} = \begin{cases} t & \text{with } t \in [-1,1], \text{ 200 samples} \\ 0 \\ 0 \end{cases} \tag{32}$$

$$\mathrm{OxOy+} = \begin{cases} t & \text{with } t \in [-1,1], \text{ 200 samples} \\ 1 \\ 0 \end{cases} \tag{33}$$

$$\mathrm{Oy} = \begin{cases} 0 \\ t & \text{with } t \in [-1,1], \text{ 200 samples} \\ 0 \end{cases} \tag{34}$$

$$\mathrm{Oz} = \begin{cases} 0 \\ 0 \\ t & \text{with } t \in [-1,1], \text{ 200 samples} \end{cases} \tag{35}$$

$$\text{OzD} = \begin{cases} -0.126 \\ 0.55 \\ t & \text{with } t \in [-1, 1], \text{ 400 samples} \end{cases} \tag{36}$$

$$\text{RD} = \begin{cases} t\cos(22.5\pi/180) \\ t\sin(22.5\pi/180) \\ 0.147 & \text{with } t \in [0, 1], \text{ 400 samples} \end{cases} \tag{37}$$

$$\text{OTheta} = \begin{cases} 0.5\cos(t) \\ 0.5\sin(t) \\ 0 & \text{with } t \in [-\pi/2, \pi/2], \text{ 750 samples} \end{cases} \tag{38}$$

$$\text{ThetaBis} = \begin{cases} 0.5\cos(t) \\ 0.5\sin(t) \\ 0.125 & \text{with } t \in [-\pi/2, \pi/2], \text{ 750 samples} \end{cases} \tag{39}$$

$$\text{ThetaD} = \begin{cases} 0.5\cos(t) \\ 0.5\sin(t) \\ -0.206 & \text{with } t \in [-\pi/2, \pi/2], \text{ 750 samples} \end{cases} \tag{40}$$

$$\text{Diag} = \begin{cases} t & \text{with } t \in [-1, 1], \text{ 350 samples} \\ t & \text{idem} \\ t & \text{idem} \end{cases} . \tag{41}$$

The validation paths are depicted in Fig. 11.

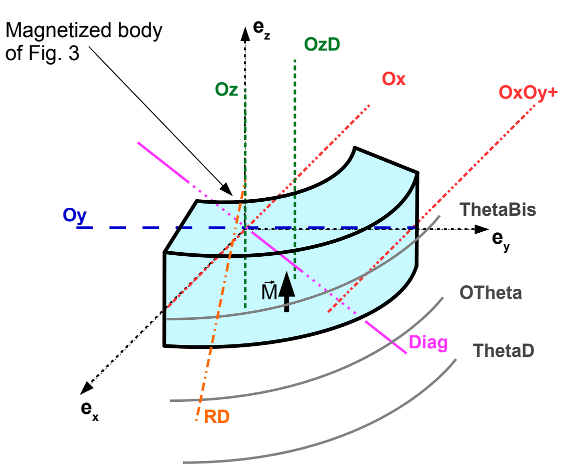


Fig. 11: Schematic representation of the validation paths used to validate the novel expressions.

## REFERENCES


[1] L. Urankar, "Vector potential and magnetic field of current-carrying finite arc segment in analytical form, Part III: Exact computation for rectangular cross section," *IEEE Trans. Magn.*, vol. 18, no. 6, pp. 1860–1867, Nov 1982.

[2] B. Marcusson and U. Lundin, "Axial magnetic fields at the ends of a synchronous generator at different points of operation," *IEEE Trans. Magn.*, vol. 51, no. 2, pp. 1–8, Feb 2015.

[3] O. Laldin, S. D. Sudhoff, and S. Pekarek, "Magnetizing end-effects in salient pole machines," *IEEE Trans. Energy Convers.*, vol. 30, no. 3, pp. 1135–1136, Sep 2015.

[4] H. Yeo, H. Park, J. Seo, S. Jung, J. Ro, and H. Jung, "Electromagnetic and thermal analysis of a surface-mounted permanent-magnet motor with overhang structure," *IEEE Trans. Magn.*, vol. 53, no. 6, pp. 1–4, Jun 2017.

[5] H. Yeo and J. Ro, "Novel analytical method for overhang effects in surface-mounted permanent-magnet machines," *IEEE Access*, vol. 7, pp. 148 453–148 461, 2019.

[6] H. Yeo, D. Lim, and H. Jung, "Magnetic equivalent circuit model considering the overhang structure of an interior permanent-magnet machine," *IEEE Trans. Magn.*, vol. 55, no. 6, pp. 1–4, Jun 2019.

[7] J. Seo, I. Jung, H. Jung, and J. Ro, "Analysis of overhang effect for a surface-mounted permanent magnet machine using a lumped magnetic circuit model," *IEEE Trans. Magn.*, vol. 50, no. 5, pp. 1–7, May 2014.

[8] H. Kwon, H. Yeo, and H. Jung, "Influence of a novel flux-absorbing structure on the performance of a surface-mounted permanent-magnet motor with overhang," *IET Elect. Power Appl.*, vol. 13, no. 12, pp. 2096–2102, 2019.

[9] R. Tsunata, M. Takemoto, S. Ogasawara, A. Watanabe, T. Ueno, and K. Yamada, "Development and evaluation of an axial gap motor using neodymium bonded magnet," *IEEE Trans. Ind. Appl.*, vol. 54, no. 1, pp. 254–262, Jan 2018.

[10] H. Park, H. Jung, S. Jung, Y. Chae, and D. Woo, "Field reconstruction method in axial flux permanent magnet motor with overhang structure," *IEEE Trans. Magn.*, vol. 53, no. 6, pp. 1–4, Jun 2017.

[11] I. P. Wiltuschnig, P. R. Eckert, D. G. Dorrell, and A. F. Flores Filho, "A study of the influence of quasi-halbach arrays on a torus machine," *IEEE Trans. Magn.*, vol. 52, no. 7, pp. 1–4, Jul 2016.

[12] P. Jin, Y. Yuan, Q. Xu, S. Fang, H. Lin, and S. L. Ho, "Analysis of axial-flux halbach permanent-magnet machine," *IEEE Trans. Magn.*, vol. 51, no. 11, pp. 1–4, Nov 2015.

[13] H. Wang, Y. Ye, Q. Wang, Y. Dai, Y. Yu, and P. Weng, "Analysis for ring arranged axial field halbach permanent magnets," *IEEE Trans. Appl. Superconduct.*, vol. 16, no. 2, pp. 1562–1565, Jun 2006.

[14] X. Wang, W. Pang, P. Gao, and X. Zhao, "Electromagnetic design and analysis of axial flux permanent magnet generator with unequal-width pcb winding," *IEEE Access*, vol. 7, pp. 164 696–164 707, 2019.

[15] S. G. Min and B. Sarlioglu, "Fast and systematic design optimization of surface-mounted pm machines using advanced analytical models and subharmonic elimination methods," *IEEE Trans. Magn.*, vol. 55, no. 1, pp. 1–16, Jan 2019.

[16] P. Virti, M. Vrai, and G. Papa, "Design of an axial flux permanent magnet synchronous machine using analytical method and evolutionary optimization," *IEEE Trans. Energy Convers.*, vol. 31, no. 1, pp. 150–158, Mar 2016.

[17] P. Virtic, P. Pisek, M. Hadziselimovic, T. Marcic, and B. Stumberger, "Torque analysis of an axial flux permanent magnet synchronous machine by using analytical magnetic field calculation," *IEEE Trans. Magn.*, vol. 45, no. 3, pp. 1036–1039, Mar 2009.

[18] Y. Shahbazi Ayat and M. R. Alizadeh Pahlavani, "3d computation of no-load magnetic flux density in slotless axial-flux permanent-magnet synchronous machines using conformal mapping," *IET Elect. Power Appl.*, vol. 11, no. 8, pp. 1391–1396, 2017.

[19] Y. N. Zhilichev, "Three-dimensional analytic model of permanent magnet axial flux machine," *IEEE Trans. Magn.*, vol. 34, no. 6, pp. 3897–3901, Nov 1998.

[20] E. P. Furlani and M. A. Knewtson, "A three-dimensional field solution for permanent-magnet axial-field motors," *IEEE Trans. Magn.*, vol. 33, no. 3, pp. 2322–2325, May 1997.

[21] Y. Huang, B. Ge, J. Dong, H. Lin, J. Zhu, and Y. Guo, “3-d analytical modeling of no-load magnetic field of ironless axial flux permanent magnet machine,” *IEEE Trans. Magn.*, vol. 48, no. 11, pp. 2929–2932, Nov 2012.

[22] P. Jin, Y. Yuan, J. Minyi, F. Shuhua, L. Heyun, H. Yang, and S. L. Ho, “3-d analytical magnetic field analysis of axial flux permanent-magnet machine,” *IEEE Trans. Magn.*, vol. 50, no. 11, pp. 1–4, Nov 2014.

[23] M. K. Ghosh, Y. Gao, H. Dozono, K. Muramatsu, W. Guan, J. Yuan, C. Tian, and B. Chen, “Proposal of maxwell stress tensor for local force calculation in magnetic body,” *IEEE Trans. Magn.*, vol. 54, no. 11, pp. 1–4, Nov 2018.

[24] H. S. Choi, I. H. Park, and S. H. Lee, “Generalized equivalent magnetizing current method for total force calculation of magnetized bodies in contact,” *IEEE Trans. Magn.*, vol. 42, no. 4, pp. 531–534, Apr 2006.

[25] J. E. Pasciak, “A new scalar potential formulation of the magnetostatic field problem,” *Math. Comp.*, vol. 43, no. 168, pp. 433–445, 1984.

[26] T. Fukushima, “Fast computation of jacobian elliptic functions and incomplete elliptic integrals for constant values of elliptic parameter and elliptic characteristic,” *Celest. Mech. Dyn. Astronomy*, vol. 105, no. 1-3, p. 245, 2009.

[27] ——, “Precise and fast computation of a general incomplete elliptic integral of third kind by half and double argument transformations,” *J. Comp. Appl. Mathemat.*, vol. 236, no. 7, pp. 1961–1975, 2012.

[28] ——, “Fast computation of a general complete elliptic integral of third kind by half and double argument transformations,” *J. Comp. Appl. Mathemat.*, vol. 253, pp. 142–157, 2013.

[29] L. Urankar, “Common compact analytical formulas for computation of geometry integrals on a basic cartesian sub-domain in boundary and volume integral methods,” *Eng. analysis with boundary elements*, vol. 7, no. 3, pp. 124–129, 1990.

[30] H. L. Rakotoarison, J. . Yonnet, and B. Delinchant, “Using coulombian approach for modeling scalar potential and magnetic field of a permanent magnet with radial polarization,” *IEEE Trans. Magn.*, vol. 43, no. 4, pp. 1261–1264, Apr 2007.

[31] E. P. Furlani, S. Reznik, and A. Kroll, “A three-dimensional field solution for radially polarized cylinders,” *IEEE Trans. Magn.*, vol. 31, no. 1, pp. 844–851, Jan 1995.

[32] R. Ravaud, G. Lemarquand, V. Lemarquand, and C. Depollier, “Discussion about the analytical calculation of the magnetic field created by permanent magnets,” *Prog. Electromagn. Res. B*, vol. 11, pp. 281–297, 2009.

[33] S. I. Babic and C. Akyel, “Improvement in the analytical calculation of the magnetic field produced by permanent magnet rings,” *Progr. Electromagn. Res.*, vol. 5, pp. 71–82, 2008.

[34] L. Jian and K.-T. Chau, “Analytical calculation of magnetic field distribution in coaxial magnetic gears,” *Progr. Electromagn. Res.*, vol. 92, pp. 1–16, 2009.

[35] J. P. Selvaggi, S. Salon, O. . Kwon, and M. V. K. Chari, “Computation of the three-dimensional magnetic field from solid permanent-magnet bipolar cylinders by employing toroidal harmonics,” *IEEE Trans. Magn.*, vol. 43, no. 10, pp. 3833–3839, Oct 2007.

[36] R. Ravaud, G. Lemarquand, and V. Lemarquand, “Magnetic field created by tile permanent magnets,” *IEEE Trans. Magn.*, vol. 45, no. 7, pp. 2920–2926, Jul 2009.

[37] R. Ravaud, G. Lemarquand, V. Lemarquand, and C. Depollier, “Analytical calculation of the magnetic field created by permanent-magnet rings,” *IEEE Trans. Magn.*, vol. 44, no. 8, pp. 1982–1989, Aug 2008.

[38] ——, “Permanent magnet couplings: Field and torque three-dimensional expressions based on the coulombian model,” *IEEE Trans. Magn.*, vol. 45, no. 4, pp. 1950–1958, Apr 2009.

[39] R. Ravaud and G. Lemarquand, “Comparison of the coulombian and amperian current models for calculating the magnetic field produced by radially magnetized arc-shaped permanent magnets,” *Prog. Electromagn. Res.*, vol. 95, pp. 309–327, 2009.

[40] P. Byrd and M. Friedman, “Handbook of elliptic integrals for engineers and scientists (; berlin,” 1971.

[41] F. Maurer, B. Kawkabani, and J. K. Nøland, “Rapid 3-d magnetic integral field computation of current-carrying finite arc segments with rectangular cross section,” *IEEE Trans. Magn.*, vol. 56, no. 2, pp. 1–12, Feb 2020.

# APPENDIX A
# BIOGRAPHIES

**Frederic Maurer** received his master degree in 2009 and the Ph.D. degree in 2019 from the Swiss Federal Institute of Technology in Lausanne (EPFL). Since april 2009, he is working for Alstom Hydro (now GE Hydro) in different position: R&D engineer in the generator technology center, Lead electrical engineer and technical project manager.

**Basile Kawkabani** (M'00-SM'11) received the master's degree from Ecole Superieure d'Electricite (SUPELEC), Paris, France, in 1978, and the Ph.D. degree in electrical engineering from the Ecole Polytechnique Federale de Lausanne (EPFL), Lausanne, Switzerland, in 1984. From 1992 to 2010, he was a Lecturer and Research Associate in electrical machines at the Electrical Machinery Laboratory, EPFL and till April 2017 a Senior Scientist at EPFL.

**Jonas Kristiansen Nøland** (S'14-M'17) received the Ph.D. degree in engineering physics from Uppsala University, Uppsala, Sweden, in 2017. He is currently an Associate Professor with the Department of Electric Power Engineering, Norwegian University of Science and Technology, Trondheim, Norway. His research interests include excitation systems, large AC machines for aviation, magnetic levitation and electric transportation. Dr. Nøland is currently serving as an Editor for the IEEE TRANSACTIONS ON ENERGY CONVERSION.